coatings

MDPI

Article

Contamination Particles and Plasma Etching Behavior of Atmospheric Plasma Sprayed Y_2O_3 and YF_3 Coatings under NF_3 Plasma

Je-Boem Song [1,2,†], Jin-Tae Kim [1,†], Seong-Geun Oh [2] and Ju-Young Yun [1,*]

[1] Materials and Energy Measurement Center, Korea Research Institute of Standards and Science (KRISS), Daejeon 34113, Korea; sjb@kriss.re.kr (J.-B.S.); kimjt@kriss.re.kr (J.-T.K.)
[2] Department of Chemical Engineering, Hanyang University, Seoul 04763, Korea; seongoh@hanyang.ac.kr
* Correspondence: jyun@kriss.re.kr; Tel.: +82-42-868-5669
† These authors contributed equally to this study.

Received: 26 December 2018; Accepted: 1 February 2019; Published: 7 February 2019

Abstract: Yttrium oxide (Y_2O_3) and yttrium oxyfluoride ($YO_{0.6}F_{2.1}$) protective coatings were prepared by an atmospheric plasma spraying technique. The coatings were exposed to a NF_3 plasma. After the NF_3 plasma treatment, the mass loss of the coatings showed that the etching rate of $YO_{0.6}F_{2.1}$ was larger than that of the Y_2O_3. X-ray photoelectron spectroscopy revealed that $YO_{0.5}F_{1.9}$ was present in the Y_2O_3 coating, whereas $YO_{0.4}F_{2.2}$ was present in the $YO_{0.6}F_{2.1}$ coating. Transmission electron microscope analysis conducted on contamination particles generated during the plasma etching showed that both coatings were mainly composed of YF_x. The contamination particles estimated by in-situ particle monitoring sensor revealed that the $YO_{0.6}F_{2.1}$ compared with the Y_2O_3 coatings produced 65% fewer contamination particles.

Keywords: yttrium oxide (Y_2O_3); yttrium oxyfluoride (YOF); yttrium fluoride (YF_3); atmospheric plasma spraying (APS); contamination particle; plasma etching; NF_3 plasma

---

1. Introduction

Plasmas are widely used for etching and cleaning in the semiconductor and display industries. Ceramic parts such as electrodes, shower heads, liners, and focusing rings used in these processes are exposed to the plasma. These parts erode and produce contamination particles, which cause serious problems, such as lowering the yield of mass-production [1–5]. In particular, when the dual frequency coupled plasma is applied, the showerhead in the position facing the wafer is heavily etched in a high flux of plasma [6–10]. Corrosion can be minimized with the use of ceramic coatings, which have outstanding plasma resistance. Yttrium oxide (Y_2O_3) is widely used as a coating material, owing to is low etching rate and low chemical reactivity. Recently, YOF and YF_3 coatings have been reported as a new candidate, which can inhibit chemical reactions with fluorine gases, such as CF_4, SF_6, and NF_3. The etching characteristics of fluorocarbon gases, such as CF_4 and C_2F_6, have been widely studied. However, etching with these gases is often accompanied by the formation of an unnecessary fluorocarbon polymer layer; hence, NF_3 gas is used as an alternative to fluorocarbon gases. Another advantage is that NF_3 is almost fully dissociated in the discharge, which results in a high etching rate [11–14]. The erosion behaviors of Y_2O_3, YOF, and YF_3 coatings in $CF_4/O_2/Ar$ plasmas have been reported in previous works [15–34]. However, there have been no studies on the corrosion behavior of the yttrium-based materials or contamination particles generated from them in NF_3 plasmas. In this study, we examine and compare the etching behavior and the generation of contamination particles in an NF_3 plasma from Y_2O_3 and $YO_{0.6}F_{2.1}$ coatings, fabricated by atmospheric plasma spraying (APS).

2. Experimental

The disc-like substrates were made of Al alloy 6061 and had a diameter of 76 mm and thickness of 3 mm. The substrates were then coated with Y_2O_3 and $YO_{0.6}F_{2.1}$ by atmospheric plasma spraying (APS) [23–31], with the use of a plasma spray system (Mettech's Axial III, Northwest Mettech Corp., North Vancouver, BC, Canada), where the Y_2O_3 and YF_3 were in a powder form (99.99%, D50 = 30 μm, Shin-Etsu, Tokyo, Japan). The sprayed coatings of Y_2O_3 and $YO_{0.6}F_{2.1}$ were respectively 110 and 70 μm thick. The APS coating was performed as follows; the Ar, N_2, and H_2 at flow rates were 80, 80, and 20 L/min, respectively, were used to generate a plasma arc and the plasma arc current was 230 A.

Figure 1 shows a schematic diagram of the capacitively coupled plasma system. A specimen was placed in the upper electrode, as shown in Figure 1. The NF_3 gas was used for plasma generation and was supplied through a showerhead with a mass flow controller. Magnets were inserted in the upper electrode to enhance the plasma density. A dry pump and turbo pump were used in the vacuum system and the working pressure of the experiment was 26.6 Pa. The power was set to be 13.56 MHz (Sizer Generator, Advanced Energy, Fort Collins, CO, USA), and an impedance matching network (Navigator, Advanced Energy, Fort Collins, CO, USA) was used to deliver the maximum power. The RF power applied to the plasma was 400 W. Before and after the NF_3 plasma etching, the surface morphology and composition of the Y_2O_3 and $YO_{0.6}F_{2.1}$ coatings were analyzed by the field-emission scanning electron microscopy (FE-SEM, S-4800, Hitachi, Tokyo, Japan) and X-ray photoelectron spectroscopy (XPS) (Monochromatic Al-Kα, AXIS-NOVA, Manchester, UK), respectively. The mass of the specimen was measured before and after the plasma etching test using a XP205 analytical balance (Mettler Toledo, Greifensee, Switzerland). After plasma etching was performed for 10 min, the specimen was taken out and the mass loss was measured. This procedure was repeated until the accumulated plasma exposure time was 60 min.

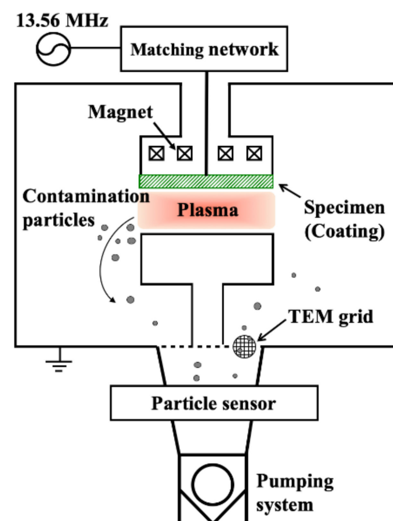

Figure 1. Schematic diagram of capacitively coupled plasma (CCP) etching system.

The contamination particles produced from the Y_2O_3 and $YO_{0.6}F_{2.1}$ coatings were measured in real time according to the NF_3 plasma exposure time. A light scattering sensor ISPM (Stiletto, In Situ Particle Monitor, Inficon, Heidiland, Switzerland) was attached to the exhaust line to measure the amount and size of the contamination particles. This system was capable of measuring contamination particles in real time as they passed through the exhaust pipe. The minimum measurable particle size was ~0.2 μm. The sensor was based on the principles of laser light scattering, and more details of its working principles can be found in previous reports [35,36]. The contamination particles generated during the plasma etching were collected on a TEM grid and observed for shape and composition under a transmission electron microscope (TEM, Taitan 300 K, Renton, WA, USA). As shown in Figure 1, the TEM grid was placed at the bottom of the chamber.

3. Results and Discussion

Figure 2 shows FE-SEM images of the surface of Y_2O_3 and $YO_{0.6}F_{2.1}$ coatings before and after exposure to NF_3 plasma; Figure 2a,b for Y_2O_3 and Figure 2c,d for $YO_{0.6}F_{2.1}$. Before NF_3 plasma etching, the surfaces of the Y_2O_3 and $YO_{0.6}F_{2.1}$ coatings had a similar rough surface. After plasma etching, the Y_2O_3 coating showed more cavities than the $YO_{0.6}F_{2.1}$ coating, as denoted in Figure 2b. This result is consistent with a recent report [29]. Figure 3 shows the mass loss of Y_2O_3 and $YO_{0.6}F_{2.1}$ vs. the NF_3 plasma etching time. The $YO_{0.6}F_{2.1}$ coating was etched more than the Y_2O_3 coating. The etch rates of the Y_2O_3 and $YO_{0.6}F_{2.1}$ coatings were ~29 and 117 nm/min/m^2, respectively. After the plasma exposure of the coatings, the amounts of Y (Yttrium), O (Oxygen) and F (Fluorine) were measured by XPS analysis. The results are presented in Table 1. Compared to a before etching specimen, the Y_2O_3 coating on the electrode after plasma exposure had less O, but more F. This result not surprising and is consistent with previous studies [29–31].

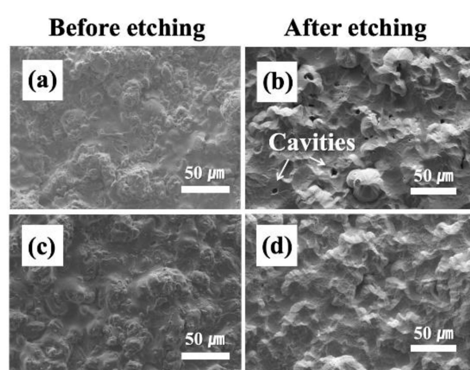

Figure 2. FE-SEM images of the surface of Y_2O_3 and $YO_{0.6}F_{2.1}$ coatings before and after exposure to NF_3 plasma; (**a**) Y_2O_3 and (**c**) $YO_{0.6}F_{2.1}$ before etching, (**b**) Y_2O_3 and (**d**) $YO_{0.6}F_{2.1}$ after etching.

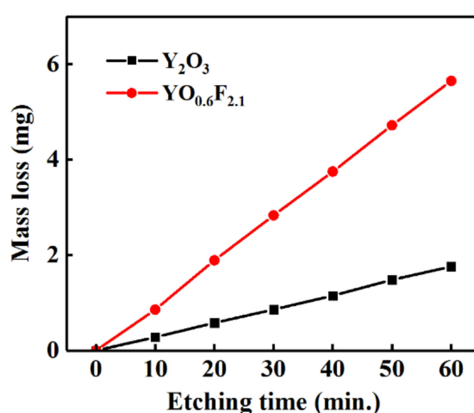

Figure 3. Mass loss owing to NF_3 plasma etching: Y_2O_3 and $YO_{0.6}F_{2.1}$ coatings.

Table 1. XPS analysis results of Y_2O_3 and $YO_{0.6}F_{2.1}$ coatings before and after exposure to the NF_3 plasma.

Compound Content (at.%)	Y_2O_3 Coating		$YO_{0.6}F_{2.1}$ Coating	
	Before Etching	After Etching	Before Etching	After Etching
Yttrium (Y3*d*)	28.3	29.2	26.9	27.3
Oxygen (O1*s*)	70.3	15.0	16.8	11.8
Fluorine (F1*s*)	1.4	55.8	56.3	60.9

Figure 4 shows the XPS spectra for yttrium in Y_2O_3 and $YO_{0.6}F_{2.1}$ before and after the plasma treatment. We assigned dash lines the peaks in the XPS spectra to the cations of $Y3d_{5/2}$ and $Y3d_{3/2}$.

The two peaks had a difference of 2.05 eV with an intensity ratio of 3:2 in their binding energy, which is consistent with the figure provided by national institute of standards and technology (NIST) [37]. In the case of pristine Y_2O_3, the Y3$d_{5/2}$ peak positions were 157.35 and 156 eV, and the Y3$d_{3/2}$ peak positions were 159.4 and 158.05 eV. When Y_2O_3 was exposed to the NF_3 plasma, XPS analysis revealed binding energies of 158.65 eV for Y3$d_{5/2}$ and 160.7 eV for Y3$d_{3/2}$, which indicated binding of yttrium to fluorine and formation of Y–F bonds. Figure 4a consists of three Y–O peaks located at 159.4, 158.05, and 156 eV. As shown in Figure 4c, the peak shifted to higher energy could be attributed to the Y–F bond, which is possibly attributed to the different electronegativity of fluorine and oxygen atoms. When the oxygen atoms around the cations are replaced by fluorine atoms, more electrons transferred to fluorine. Therefore, the electron density around the cation decreases and the binding energy is enhanced [20]. This result indicates that the surface of Y_2O_3 reacted with fluorine radicals and was composed of $YO_{0.5}F_{1.9}$. However, the $YO_{0.6}F_{2.1}$ coating showed less change in the composition after the plasma treatment.

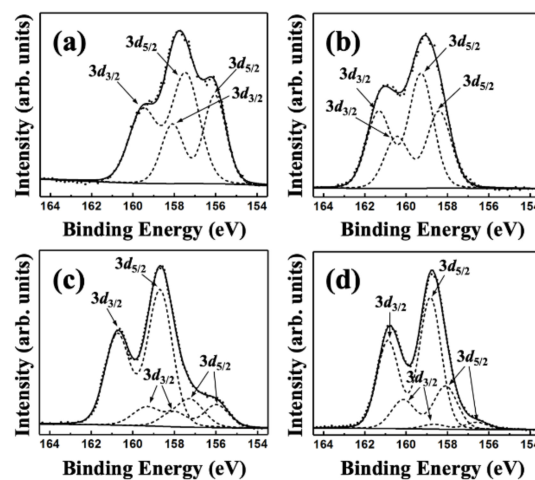

Figure 4. Peak positions of the XPS spectra of the surface; (**a**) Y_2O_3 and (**b**) $YO_{0.6}F_{2.1}$ before etching, (**c**) Y_2O_3 and (**d**) $YO_{0.6}F_{2.1}$ after etching.

Figure 5 shows the real-time concentration of accumulated contamination particles generated from the Y_2O_3 and $YO_{0.6}F_{2.1}$ coatings during the NF_3 plasma treatment of 60 min. The $YO_{0.6}F_{2.1}$ coating produced fewer contamination particles than did the Y_2O_3 coating; the concentration of particles measuring over 0.2 μm from the $YO_{0.6}F_{2.1}$ coating was less than 65% that of the Y_2O_3 coating. Figure 6 shows the distribution of the sum of contamination particles from Figure 5. Most contamination particles had sizes falling in the range of 0.2 to 0.5 μm. The etching rate of $YO_{0.6}F_{2.1}$ was higher than that of Y_2O_3 in NF_3 plasma. However, $YO_{0.6}F_{2.1}$ produced less contamination particle than Y_2O_3. This can be explained as follows. The boiling temperature of Y_2O_3 and YF_3 are 4570 and 2500 K, respectively. In addition, the sublimation enthalpies of Y_2O_3 are also higher than that of YF_3. Hence, Y_2O_3 is more stable and more difficult to vaporize than YF_3. Therefore, its sputtering yield by ion bombardment may be lower for the Y_2O_3 than for the YF_3 containing a relatively large amount of oxygen. This is consistent with the result of Reference 17 and 30, where the etching rate differences depend on the bias voltage [17,30]. On the surface of Y_2O_3, YO_xF_y layer and volatile NO_x are formed by the chemical reaction with the fluorine radical. On the other hand, YO_xF_y layer and NO_x can be formed less on the surface of $YO_{0.6}F_{2.1}$ because Y–F bond already exists. Also, the less oxygen on the coating surface, the smaller the chemical reaction. Thus, the Y_2O_3 surface provides a more appropriate environment for the growth of YO_xF_y (or YF_3) contamination particles, and, therefore, more contamination particles from Y_2O_3 are generated compared to $YO_{0.6}F_{2.1}$ [28,29]. Furthermore, in the case of $YO_{0.6}F_{2.1}$ surface, physical etching is more likely to occur than chemical etching by fluorine radical. $YO_{0.6}F_{2.1}$ is relatively inadequate to grow YF_3 contamination particle compared to Y_2O_3.

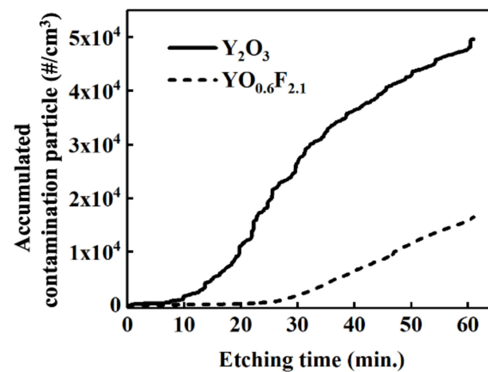

Figure 5. Real-time detection of accumulated contamination particle concentration, over 0.2 µm size, generated from Y_2O_3 and $YO_{0.6}F_{2.1}$ during the 60 min NF_3 plasma treatment.

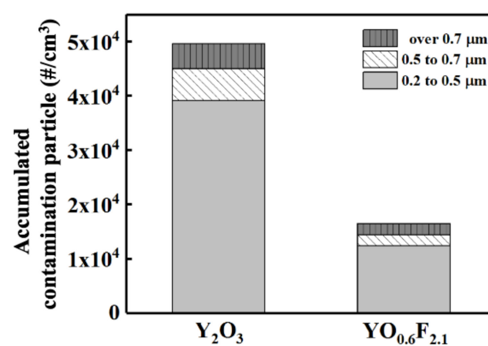

Figure 6. Size distribution of contamination particles, over 0.2 µm size, generated from Y_2O_3 and $YO_{0.6}F_{2.1}$ during the 60 min NF_3 plasma treatment.

Figure 7 shows TEM images of particles that detached from the coatings during plasma etching. The particles were of various sizes, and the selected particle was approximately 500 nm in size. The particles that fell off the Y_2O_3 and $YO_{0.6}F_{2.1}$ coatings had irregular shapes and crystalline structures. In addition to observing particle shapes by TEM, we used energy dispersive X-ray spectroscopy (EDS) to examine their composition. These results are listed in Table 2. The contamination particles derived from Y_2O_3 and $YO_{0.6}F_{2.1}$ contained almost no oxygen and their chemical composition was most likely YF_x, and rather close to YF_3, which is consistent with Reference [29–31].

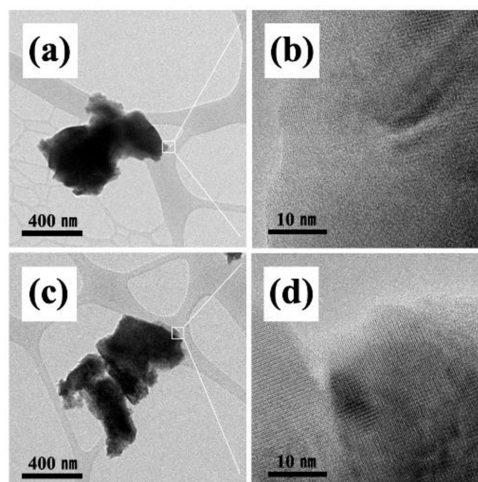

Figure 7. TEM images of contamination particles; (**a**,**b**) generated from Y_2O_3 and (**c**,**d**) generated in $YO_{0.6}F_{2.1}$.

Table 2. EDS analysis results of contamination particles generated in Y_2O_3 and $YO_{0.6}F_{2.1}$ coatings after exposure to the NF_3 plasma.

Compound Content (wt.%)	Particle Generated in Y_2O_3 Coating	Particle Generated in $YO_{0.6}F_{2.1}$ Coating
Yttrium	63.5	61.8
Oxygen	0.8	0.6
Fluorine	35.7	37.6

4. Conclusions

We exposed Y_2O_3 and $YO_{0.6}F_{2.1}$ coatings prepared by atmospheric plasma spraying (APS) to NF_3 plasma. Both coatings had rough surfaces in the pristine state, and no differences were observed between the two. When subjected to a NF_3 plasma treatment, the Y_2O_3 coating showed many defects, and cavities formed in the coatings whereas the $YO_{0.6}F_{2.1}$ coating did form any cavities. We estimated the etching rates of Y_2O_3 and $YO_{0.6}F_{2.1}$ coatings from the mass loss to be ~29 and 117 nm/min/m^2, respectively. During etching, the surface of Y_2O_3 reacted with fluorine radicals to form particles composed of YO_xF_y and YF_x. However, particles from the $YO_{0.6}F_{2.1}$ coating showed almost no change in composition. Fewer contamination particles over 0.2 µm size were generated for the $YO_{0.6}F_{2.1}$ coating than for the Y_2O_3 coating. The particles produced from both coatings had irregular shapes, mainly consisting of YF_x, with a composition close to YF_3. These results indicate that the fluorine radicals replaced oxygen at the Y_2O_3 surface such that YF_x particles were formed. The $YO_{0.6}F_{2.1}$ coating did not provide conditions suitable for YF_x particles to grow. This study demonstrates that the $YO_{0.6}F_{2.1}$ coating might be used by the semiconductor industry as a candidate material to reduce contamination particles over 0.2 µm size.

Author Contributions: Conceptualization, J.-B.S. and J.-T.K.; Methodology, J.-B.S.; Investigation, J.-B.S.; Writing—Original Draft Preparation, J.-B.S. and J.-T.K.; Writing—Review and Editing, S.-G.O. and J.-Y.Y.; Supervision, S.-G.O. and J.-Y.Y.

Funding: This research was funded by the R&D Convergence Program of National Research Council of Science and Technology (NST) of the Republic of Korea (NST, CAP-16-04-KRISS) and Korea Research Institute of Standards and Science (KRISS-2018-GP2018-0011).

Conflicts of Interest: The authors declare no conflict of interest.

References

1. Coburn, J.W.; Winters, H.F. Plasma etching-A discussion of mechanisms. *J. Vac. Sci. Technol.* **1979**, *16*, 391–403. [CrossRef]
2. Donnelly, V.M.; Kornblit, A. Plasma etching: Yesterday, today, and tomorrow. *J. Vac. Sci. Technol. A Vac. Surf. Films* **2013**, *31*, 050825. [CrossRef]
3. Abe, H.; Yoneda, M.; Fujiwara, N. Developments of plasma etching technology for fabricating semiconductor devices. *Jpn. J. Appl. Phys.* **2008**, *47*, 1435. [CrossRef]
4. Ito, N.; Moriya, T.; Uesugi, F.; Matsumoto, M.; Liu, S.; Kitayama, Y. Reduction of particle contamination in plasma-etching equipment by dehydration of chamber Wall. *Jpn. J. Appl. Phys.* **2008**, *47*, 3630. [CrossRef]
5. Kasashima, Y.; Natsuko, N.; Uesugi, F. Instantaneous generation of many flaked particles by impulsive force of electric field stress acting on inner wall of mass-production plasma etching equipment. *Jpn. J. Appl. Phys.* **2013**, *52*, 066201. [CrossRef]
6. Babaeva, N.Y.; Kushner, M.J. Ion energy and angular distributions into the wafer-focus ring gap in capacitively coupled discharges. *J. Phys. D Appl. Phys.* **2008**, *41*, 062004. [CrossRef]
7. Sung, D.; Jeong, S.; Park, Y.; Volynets, V.N.; Ushakov, A.G.; Kim, G.H. Effect on plasma and etch-rate uniformity of controlled phase shift between rf voltages applied to powered electrodes in a triode capacitively coupled plasma reactor. *J. Vac. Sci. Technol. A Vac. Surf. Films* **2009**, *27*, 0734. [CrossRef]
8. Yang, Y.; Kushner, M.J. Modeling of dual frequency capacitively coupled plasma sources utilizing a full-wave Maxwell solver: I. Scaling with high frequency. *Plasma Sources Sci. Technol.* **2010**, *19*, 055011. [CrossRef]

9. Yang, Y.; Kushner, M.J. Modeling of dual frequency capacitively coupled plasma sources utilizing a full-wave Maxwell solver: II. Scaling with pressure, power and electronegativity. *Plasma Sources Sci. Technol.* **2010**, *19*, 055012. [CrossRef]
10. Schulze, J.; Schungel, E.; Donko, Z.; Czarnetzki, U. Charge dynamics in capacitively coupled radio frequency discharges. *J. Phys. D Appl. Phys.* **2010**, *43*, 225201. [CrossRef]
11. Machima, P.; Hershkowitz, N. SiO_2 and Si_3N_4 etch mechanisms in NF_3/hydrocarbon plasma. *J. Phys. D Appl. Phys.* **2006**, *39*, 673. [CrossRef]
12. Ji, B.; Yang, J.H.; Badowski, P.R.; Karwacki, E.J. Optimization and analysis of NF_3 in situ chamber cleaning plasmas. *J. Appl. Phys.* **2004**, *95*, 4452–4462. [CrossRef]
13. Kastenmeir, B.E.E.; Matsuo, P.J.; Oehrlein, G.S.; Langan, J.G. Remote plasma etching of silicon nitride and silicon dioxide using NF_3/O_2 gas mixtures. *J. Vac. Sci. Technol. A Vas. Surf. Films* **1998**, *16*, 2047–2056. [CrossRef]
14. Matsuo, P.J.; Kastenmeier, B.E.E.; Oehrlein, G.S.; Langan, J.G. Silicon etching in NF_3/O_2 remote microwave plasmas. *J. Vac. Sci. Technol. A Vas. Surf. Films* **1999**, *17*, 2431–2434. [CrossRef]
15. Shin, J.S.; Kim, M.; Song, J.B.; Jeong, N.G.; Kim, J.T.; Yun, J.Y. Fluorine plasma corrosion resistance of anodic oxide film depending on electrolyte temperature. *Appl. Sci. Converg. Technol.* **2018**, *27*, 9–13.
16. Zhao, D.; Wang, C.Y.; Chen, Y.; Wang, Y.G. Phase composition, structural, and plasma erosion properties of ceramic coating prepared by suspension plasma spraying. *Int. J. Appl. Ceram. Technol.* **2018**, *15*, 1388–1396. [CrossRef]
17. Cao, Y.C.; Zhao, L.; Luo, J.; Wang, K.; Zhang, B.P.; Tokota, H.; Ito, Y.; Li, J.F. Plasma etching behavior of Y_2O_3 ceramics: Comparative study with Al_2O_3. *Appl. Surf. Sci.* **2016**, *366*, 304–309. [CrossRef]
18. Song, J.B.; Kim, J.T.; Oh, S.G.; Shin, J.S.; Chun, J.R.; Yun, J.Y. Effect of sealing time of anodic aluminum oxide (AAO) film for preventing plasma damage. *Sci. Adv. Mater.* **2015**, *7*, 127–132. [CrossRef]
19. Goto, T.; Sugawa, S. Observation of sputtering of yttrium form Y_2O_3 ceramics by low-energy Ar, Kr, and Xe ion bombardment in microwave-excited plasma. *Jpn. J. Appl. Phys.* **2015**, *54*, 128003. [CrossRef]
20. Kim, D.M.; Lee, S.H.; Alexander, W.B.; Kim, K.B.; Oh, Y.S.; Lee, S.M. X-Ray photoelectron spectroscopy study on the interaction of yttrium-aluminum oxide with fluorine-based plasma. *J. Am. Ceram. Soc.* **2011**, *94*, 3455–3459. [CrossRef]
21. Choi, H.; Kim, K.; Choi, H.; Kang, S.; Yun, J.; Shin, Y.; Kim, T. Plasma resistant aluminum oxide coatings for semiconductor processing apparatus by atmospheric aerosol spray method. *Surf. Coat. Technol.* **2010**, *205*, S125–S128. [CrossRef]
22. Erkmen, Z.E.; Anghaie, S. Interaction of yttria with uranium fluoride gases (UF_n, n = 4, 6) at high temperatures. *J. Am. Ceram. Soc.* **1994**, *77*, 1624–1632. [CrossRef]
23. Tahara, R.; Tsunoura, T.; Yoshida, K.; Yano, T.; Kishi, Y. Fabrication of dense yttrium oxyfluoride ceramics by hot pressing and their mechanical, thermal, and electrical properties. *Jpn. J. Appl. Phys.* **2018**, *57*, 06JF04. [CrossRef]
24. Lin, T.K.; Wuu, D.S.; Huang, S.Y.; Wang, W.K. Preparation and characterization of sprayed-yttrium oxyfluoride corrosion protective coating for plasma process chambers. *Coatings* **2018**, *8*, 373. [CrossRef]
25. Wang, W.K.; Lin, Y.X.; Xu, Y.J. Structural and fluorine plasma etching behavior of sputter-deposition yttrium fluoride film. *Nanomaterials* **2018**, *8*, 936. [CrossRef] [PubMed]
26. Ma, T.; List, T.; Donnelly, V.M. Comparisons of NF_3 plasma-cleaned Y_2O_3, YOF, and YF_3 chamber coatings during silicon etching in Cl_2 plasmas. *J. Vac. Sci. Technol. A Vac. Surf. Films* **2018**, *36*, 0734. [CrossRef]
27. Shiba, Y.; Teramoto, A.; Goto, T.; Kishi, Y.; Shirai, Y.; Sugawa, S. Stable yttrium oxyfluoride used in plasma process chamber. *J. Vac. Sci. Technol. A Vac. Surf. Films* **2017**, *35*, 021405. [CrossRef]
28. Kim, D.M.; Jang, M.R.; Oh, Y.S.; Kim, S.; Lee, S.M.; Lee, S.H. Relative sputtering rates of oxides and fluorides of aluminum and yttrium. *Surf. Coat. Technol.* **2017**, *309*, 694–697. [CrossRef]
29. Lin, T.K.; Wang, W.K.; Huang, S.Y.; Tasi, C.T.; Wuu, D.S. Comparison of erosion behavior and particle contamination in mass-production CF_4/O_2 plasma chambers using Y_2O_3 and YF_3 protective coatings. *Nanomaterials* **2017**, *7*, 183. [CrossRef]
30. Kim, D.M.; Oh, Y.S.; Kim, S.; Kim, H.T.; Lim, D.S.; Lee, S.M. The erosion behaviors of Y_2O_3 and YF_3 coatings under fluorocarbon plasma. *Thin Solid Films* **2011**, *519*, 6698–6702. [CrossRef]

31. Lin, T.K.; Wuu, D.S.; Huang, S.Y.; Wang, W.K. Characteristics of yttrium fluoride and yttrium oxide coating for plasma process equipment prepared by atmospheric plasma spraying. *Jpn. J. Appl. Phys.* **2016**, *55*, 126201. [CrossRef]
32. Bakan, E.; VaBen, R. Ceramic top coats of plasma-sprayed thermal barrier coatings: Materials, processes, and properties. *J. Therm. Spray Technol.* **2017**, *26*, 992–1010. [CrossRef]
33. Fan, W.; Bai, Y. Review of suspension and solution precursor plasma sprayed thermal barrier coatings. *Ceram. Intern.* **2016**, *42*, 14299–14312. [CrossRef]
34. Pawlowski, L. *The Science and Engineering of Thermal Spray Coatings*; John Wiley & Sons: Chichester, UK, 2008.
35. Miyashita, H.; Kikuchi, T.; Kawasaki, Y.; Katakura, Y.; Ohsako, N. Particle measurements in vacuum tools by in situ particle monitor. *J. Vac. Sci. Technol. A Vac. Surf. Films* **1999**, *17*, 1066–1070. [CrossRef]
36. Hulst, H.C. *Light Scattering by Small Particles*; Courier Publications, Inc.: New York, NY, USA, 1981.
37. NIST X-ray Photoelectron Spectroscopy Database. Available online: https://srdata.nist.gov/xps/ (accessed on 15 September 2012).

© 2019 by the authors. Licensee MDPI, Basel, Switzerland. This article is an open access article distributed under the terms and conditions of the Creative Commons Attribution (CC BY) license (http://creativecommons.org/licenses/by/4.0/).